Optics Letters

Time-resolved four-wave-mixing spectroscopy for inner-valence transitions

Thomas Ding,[1,5] Christian Ott,[1,2] Andreas Kaldun,[1] Alexander Blättermann,[1] Kristina Meyer,[1] Veit Stooss,[1] Marc Rebholz,[1] Paul Birk,[1] Maximilian Hartmann,[1] Andrew Brown,[4] Hugo Van Der Hart,[4] and Thomas Pfeifer[1,3,6]

[1]Max-Planck-Institut für Kernphysik, Saupfercheckweg 1, Heidelberg 69117, Germany
[2]Chemistry Department, University of California, Berkeley, California 94720, USA
[3]Centre for Quantum Dynamics, Ruprecht-Karls-Universität Heidelberg, Heidelberg 69120, Germany
[4]Centre for Theoretical Atomic, Molecular and Optical Physics, Queen's University Belfast, Belfast BT7 1NN, UK
[5]e-mail: thomas.ding@mpi-hd.mpg.de
[6]e-mail: thomas.pfeifer@mpi-hd.mpg.de

Received 26 November 2015; revised 23 December 2015; accepted 30 December 2015; posted 7 January 2016 (Doc. ID 254683); published 5 February 2016

Noncollinear four-wave-mixing (FWM) techniques at near-infrared (NIR), visible, and ultraviolet frequencies have been widely used to map vibrational and electronic couplings, typically in complex molecules. However, correlations between spatially localized inner-valence transitions among different sites of a molecule in the extreme ultraviolet (XUV) spectral range have not been observed yet. As an experimental step toward this goal, we perform time-resolved FWM spectroscopy with femtosecond NIR and attosecond XUV pulses. The first two pulses (XUV-NIR) coincide in time and act as coherent excitation fields, while the third pulse (NIR) acts as a probe. As a first application, we show how coupling dynamics between odd- and even-parity, inner-valence excited states of neon can be revealed using a two-dimensional spectral representation. Experimentally obtained results are found to be in good agreement with *ab initio* time-dependent R-matrix calculations providing the full description of multielectron interactions, as well as few-level model simulations. Future applications of this method also include site-specific probing of electronic processes in molecules.

OCIS codes: (190.0190) Nonlinear optics; (020.3690) Line shapes and shifts; (300.2570) Four-wave mixing; (300.6240) Spectroscopy, coherent transient; (320.7110) Ultrafast nonlinear optics; (300.1030) Absorption.

http://dx.doi.org/10.1364/OL.41.000709

With the development of coherent femtosecond-duration laser pulses, four-wave-mixing (FWM) spectroscopy has become a versatile tool for the investigation of ultrafast dynamics in molecules and other material samples. A large body of experimental approaches for time-resolved molecular spectroscopy has been developed based on FWM phenomena, such as photon echo [1], coherent anti-Stokes Raman scattering [2], transient grating [3], and many more. The most spectroscopically comprehensive implementation of FWM is the so-called two-dimensional spectroscopy (2DS) with three temporally independent pulses that allows the correlation of excitation spectra and nonlinear-response spectra to directly measure couplings between quantum states [4,5]. Two-dimensional spectroscopy in the infrared, visible, and ultraviolet spectral ranges has enabled the exploration of vibrational [6], electronic [7], and vibronic [8] coupling dynamics in complex molecular systems. The extension of 2DS into the extreme ultraviolet (XUV) and x-ray spectral regions aims to map coupling dynamics between spatially localized inner-valence or core transitions among different sites of a quantum system. It has been theoretically discussed by Mukamel and co-workers [9,10] and is a long-awaited goal. In principle, modern free-electron laser and high-harmonic generation (HHG)-based coherent XUV and x-ray light sources can provide appropriate pulses for 2DS experiments, but key challenges are both the increased technical demands to create appropriate multi-pulse geometries in this photon energy range, as well as the intrinsically low photon flux of laboratory-based sources. Nevertheless, first steps are being made, as demonstrated in recent experiments that explore NIR- and XUV-induced transient gratings that emphasize both the spectroscopic element selectivity [11] and the enhanced spatial resolution [12] capabilities of the XUV domain.

Meanwhile, an all-optical, two-color pump-probe technique utilizing weak attosecond XUV pulses and strong few-cycle NIR pulses—often referred to as attosecond transient absorption spectroscopy (ATAS)—has opened a direct route to the measurement and control of the XUV spectral response of bound electronic transitions [13–21]. With both the XUV-NIR time delay τ and the NIR intensity I_{NIR} as continuously tunable control parameters, ATAS has a multidimensional experimental anatomy [22]. Two-dimensional (2D) time-domain spectra $S(\tau, \omega)$ measured as a function of both the XUV photoexcitation frequency ω and time delay τ exhibit a characteristic fringe pattern across coherence resonances regardless of the

specific target system [23]. The Fourier transform along the signal's pulse-delay time trace is carried out ($\tau \rightarrow \nu$) to decompose the interference pattern into a two-dimensional absorption spectrum (2DAS), $\tilde{S}(\nu, \omega)$, which exhibits diagonal regions with point-like and/or line-like peaks [13,18,22,24,25], revealing information about the dynamical pathways along which the system is driven. We recently introduced an analytical framework to understand and characterize the signatures of time-delay dependent polarization dynamics in 2D-XUV absorption spectra [23].

Thus far only *dipole-allowed* transitions were excited by a single-photon XUV pump step in ATAS. Accordingly, the interference structures observed in the 2DAS only consisted of maxima at zero or even multiples of the NIR-photon energy. Interferences at odd multiples of the NIR-photon energy would indicate couplings to additional (one-photon forbidden) channels, which could be accessed by a combination of XUV- and NIR-excitation fields, as previously applied to photo-electron spectroscopy [26,27]. Here we extend ATAS (typically a XUV and a *single* time-delayed laser pulse) into a time-resolved FWM technique, where excitation and probing by an NIR-laser pulse occurs at *two different times*. The first two pulses (XUV and weak NIR) coincide in time and are temporally separated from the strong (non-perturbative) third (NIR) pulse by the time delay τ. The interaction of a sample with the first two pulses (XUV and NIR) creates a polarization, i.e., the coherent superposition of ground and both odd- and even-parity excited states. This two-color pump step extends the coherent excitation onto states, the transition into which would be forbidden by a single XUV photon from the ground state. After the excited system has evolved freely during the time delay τ, the interaction with the strong NIR pulse generates a nonlinear (third-order) response signal by coupling between XUV-dipole-allowed and dipole-forbidden excited states. We have chosen the 2*s*-inner-valence excited states $2s^{-1}3s(^1S^e)$, $2s^{-1}3d(^1D^e)$, and $2s^{-1}3p(^1P^o)$ of neon (henceforth denoted as $3s$, $3d$, and $3p$) to perform first proof-of-principle FWM experiments. Neon provides an appropriate electronic energy-level structure for investigating resonant transitions between XUV-dipole-allowed and dipole-forbidden states, which cannot be accessed by conventional ATAS methods.

The experimental setup [see Fig. 1(a)] involves a commercial Ti:sapphire multipass amplifier with hollow-core fiber and chirped-mirror compression stages for the generation of NIR (central photon energy ~1.6 eV) sub-7-fs pulses delivered at a 4 kHz repetition rate and ~0.4 mJ pulse energy. These pulses act as driver pulses for HHG in an argon gas-filled cell (~75 mbar backing pressure) yielding short trains of attosecond pulses that are inherently phase locked to the fundamental field. The HHG spectra obtained extend continuously over the autoionizing resonance region of neon between 43 and 50 eV covering the full $2s^{-1}np$ Rydberg series [cf. the HHG absorption spectrum in Fig. 1(b)]. A piezo-driven, two-component split mirror (inner, dynamic part: gold coating; outer part: silver coating) is employed to introduce a time delay between the copropagating XUV and NIR pulses. The NIR-pulse intensity is controlled by a motorized iris aperture. Spatial beam separation between XUV and NIR is achieved by a two-part spectral bandpass filter where the outer annular part consists of a 2-μm-thin nitrocellulose membrane (1.2 mm centric hole), together with a 0.2-μm-thin aluminum foil (1.2 mm diameter) as the inner part. The central part transmits a residual NIR-photon intensity on the order of 1%–10%, which can be considered

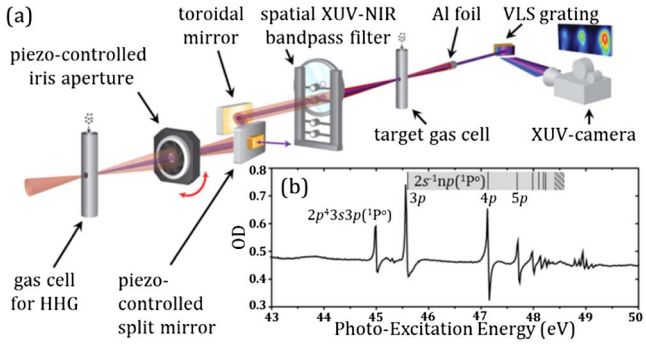

Fig. 1. (a) Schematic of the experimental setup and the key elements. Essential for creating the described pulse configuration for FWM (temporally locked XUV-NIR-excitation fields and NIR-probe field) is the piezo-controlled split mirror in combination with an annular XUV-NIR-filter geometry transmitting a residual NIR-photon flux through the inner Al filter. (b) Linear spectroscopy (XUV only): the natural neon line spectrum in terms of optical densities (OD). For more details on the experimental setup and data acquisition, see [16,17]. Resonance lines are assigned based on [39].

as a perturbative NIR-replica pulse that remains locked in temporal overlap with the XUV. The NIR transmission is due to small holes or other imperfections in the extremely fragile foil (e.g., created during the manufacturing process and/or mechanical strain while assembling the custom-made filter arrangement). Both laser beams (inner XUV-NIR and outer NIR) are focused into the neon gas-filled target cell (~35 mbar backing pressure). The transmitted XUV light contains the sample's dipole response, which is detected by a high-resolution XUV spectrometer (~20 meV Gaussian standard deviation near 45 eV, see [16] for details).

For comparison with our experimental results, calculations based on the R-matrix with time-dependence (RMT) approach [28] were carried out. RMT is an *ab initio*, nonperturbative computational technique for the description of general multielectron atomic/ionic systems interacting with a strong laser field. By employing the standard R-matrix division of space [29], a tractable solution of the time-dependent Schrödinger equation can be obtained, affording a full account of multielectron effects and a comprehensive treatment of detailed atomic structure. In order to describe both the core and doubly excited states of neon under investigation, the calculations comprise all single-, double-, and triple-excitations of the 2*s* and 2*p* electrons into $3p$, $3s$, $3d$, (spectroscopic) $\overline{4s}$ and $\overline{4p}$ (pseudo-) orbitals, which are determined as described in [30]. This leads to an expansion over 152 multielectron configurations. Additionally, to account for the various ionization pathways, six residual ion states of Ne^+ are included in the calculation. This yields energies within 0.08 eV of the literature values for the states under investigation [31–33]. Using RMT, we compute $\boldsymbol{d}(t)$: the time-dependent expectation value of the dipole operator. The absorption spectrum is then given by $\sigma(\omega) = 4\pi\omega c^{-1}\,\Im[\boldsymbol{d}(\omega)/\boldsymbol{E}(\omega)]$ [34], where ω is the photon energy, c the speed of light, and $\boldsymbol{d}(\omega)$ and $\boldsymbol{E}(\omega)$ are the Fourier transform of $\boldsymbol{d}(t)$ and the electric field, respectively.

In Figs. 2(a) and 2(b), we present time-delay-resolved absorption measurements for a scanned time delay τ between XUV-NIR pump and NIR-probe fields, obtained from experiment and RMT calculations. Absorption changes can be

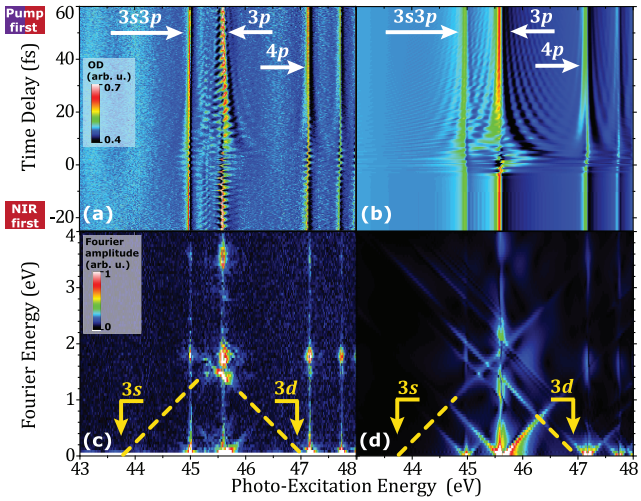

Fig. 2. (a) Time-resolved 2D absorption spectra $S(\tau, \omega)$ at $\sim 10^{12}$ W/cm^2 NIR-probe intensity obtained from experiment and (b) full *ab initio* calculations assuming Gaussian pulses and for the NIR pump 10% of the NIR-probe intensity (also see Dataset 1 in [35]). Strong periodic full-cycle modulations are imprinted on the $3p$ resonance which give rise to diagonal, line-like peaks at ~1.6 eV Fourier energy in the 2DAS, $\tilde{S}(\nu, \omega)$ (lower panels c and d, respectively), indicating coherent coupling pathways. Vertically aligned peaks are due to time-delay dependent NIR-intensity variations in the temporal overlap region. The energetic position of the dipole-forbidden $3s$ and $3d$ coupling partners ($\hbar\omega_{3s} = 43.7$ eV and $\hbar\omega_{3d} = 47.0$ eV, assignment based on [32]) are indicated by the dashed lines as a guide to the eye. Besides the excellent agreement between experiment and RMT calculations, remaining discrepancies are likely due to uncertainties in the exact experimental pulse shapes.

observed across all the resonance lines shown in Figs. 2(a) and 2(b). Our focus here is on the changes occurring near the $3p$ state at $\hbar\omega_{3p} = 45.55$ eV photo-excitation energy in order to understand the two-photon XUV-NIR-induced wave-packet dynamics created by the superposition of two coherently excited states with different parities. The time-domain absorption spectra $S(\tau, \omega)$ are Fourier analyzed ($\tau \rightarrow \nu$) to decompose the temporal beat patterns for each resonance into distinct peaks on a 2DAS, $\tilde{S}(\nu, \omega)$, spectral representation [Figs. 2(c) and 2(d)]. Peak position, shape, and orientation allow the characterization of coherent coupling and transition pathways analogous to the case previously described for XUV-only excitation and a single time-delayed NIR-probe pulse [23]. Here, the additional weak NIR pulse locked to the XUV excitation pulse plays a crucial role as it coherently excites states that would otherwise be dipole-forbidden for an XUV-only excitation. The basic structures observed in the time-domain spectra $S(\tau, \omega)$ [Figs. 2(a) and 2(b)] have been seen in several related ATAS studies with XUV-only-excitation fields [13–19,22,23,34,36–38] and can in general be decoupled into two interfering substructures [23]: *(i)*, a slow, τ-dependent modulation following a hyperbolic geometry near resonance lines corresponds to a fork-like feature with elliptically shaped peaks of slope 1 originating at zero Fourier energy in the 2DAS $\tilde{S}(\nu, \omega)$. *(ii)*, a fast τ-dependent rippling type pattern, which gives rise to line-like Fourier peaks of slope 1 at nonzero Fourier energies. According to dipole-selection rules, such Fourier peaks at even-numbered multiples of the NIR-photon energy indicate transitions between identical-parity states mediated by an even number of NIR photons. Such signatures (half- and quarter-cycle modulations) have been observed and interpreted recently [13,18,22]. In Figs. 2(c) and 2(d), we observe these Fourier features, however, at one NIR-photon energy, ~1.6 eV (full-cycle modulations), evidencing a coherent excitation and time-dependent coupling of opposite-parity states. We identify the even-parity $3s$ and $3d$ states as the coupling partners of the $3p$ state by analyzing the orientation of the two dominant line-like peaks appearing at $\hbar\omega_{3p} = 45.55$ eV photo-excitation energy and ~1.6 eV Fourier energy, which extrapolate towards the coupled resonance energies on the photo-excitation energy axis at $\hbar\omega_{3s} = 43.7$ eV and $\hbar\omega_{3d} = 47.0$ eV [32]. It is important to note that the two-color XUV-NIR pump step for the coherent excitation of both XUV-dipole-allowed and dipole-forbidden (allowed by the absorption of an additional NIR photon near time zero) transitions to final states $3p$ and $3s$, $3d$ is the key mechanism to observing Fourier features at odd-numbered multiples of the NIR-photon energy. To further confirm this understanding, we present in Fig. 3 few-level model (FLM) simulations based on the approach previously described in [16] assuming 2×10^{11} W/cm^2 NIR pump and 2×10^{12} W/cm^2 NIR-probe intensities. The numerical parameters (resonance energies, line widths, asymmetry q-parameters) used to model the three states ($3p$, $3s$, $3d$) above the ground state are taken from [32,39]. The $N = 1$ ionization continuum is not included, but we account for line-shape asymmetry effects due to continuum coupling [40] by the phase shift $\varphi(q) = 2\arg(q - i)$ of the time-dependent dipole-response function [17]. The dipole-matrix elements were estimated based on hydrogen-like orbitals, including a semi-empirical shielding of the nuclear charge by the partially filled inner shell [41]. We note the good agreement of the FLM simulation [Fig. 3(d)] with both the experimental and the RMT spectra shown in Fig. 2, which further substantiates our understanding of the underlying mechanism as a third-order (FWM) interaction process with three excited resonances ($3p$, $3s$, $3d$). In Fig. 3, we present a schematic view of the discussed mechanism and the corresponding Feynman diagrams. In principle, this method allows the extraction of coupling strengths (dipole-matrix elements) from the experimental data, as soon as the pulse shape and intensity of the NIR pulse can be accurately determined [42].

In conclusion, we implemented the well-established, two-pulse technique of ATAS in a novel FWM scheme, where the excitation and probing by an NIR pulse occurs at different times in order to access excitation and coupling channels that otherwise would be spectroscopically hidden. This enabled a direct access to coupling dynamics between inner-valence excited states of opposite parity in neon. The FWM mechanism that underlies these dynamics was interpreted and fully understood on the basis of FLM simulations. To account for the electronic correlation of the neon atom in full dimensionality, we compared our experimental results with RMT calculations and found excellent agreement. This renders the presented methodology a promising experimental tool to investigate polarizabilities in multielectron systems [43], even in excited and metastable states of different parity on ultrafast time scales. Additionally, the method can be extended to more complex systems, including the site-specific probing of intramolecular electron dynamics and excitation transfer.

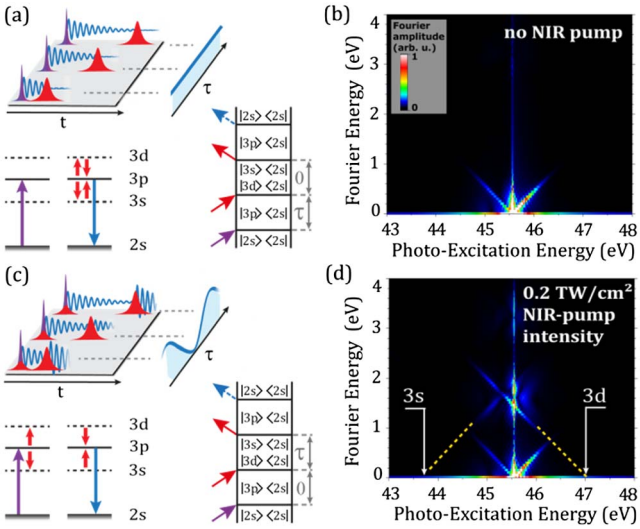

Fig. 3. Schematic illustrations and Feynman diagrams of the τ-dependent third-order coupling mechanisms (panels a and c) and corresponding FLM simulations (panels b and d). (a) The XUV pulse excites an $2s$ electron (violet arrow) creating a coherent superposition of the ground state and the $3p$ state, while XUV transitions into final states $3s$ and $3d$ are dipole-forbidden. The superposition leads to coherent dipole emission (blue wavy lines). After the time delay τ, the NIR pulse induces transient coupling (red arrows), which couples the $3p$ with the $3s$ and $3d$ states. Amplitude and phase modifications lead to the characteristic spectral features near zero Fourier energy in the 2DAS (panel b). (c) Two-photon (XUV-NIR) excitation into a coherent superposition of $3p$, $3s$, and $3d$ states. After the field-free evolution until the time delay τ, the interaction with the third (NIR) pulse mediates a coupling between these states, which leads to constructive or destructive dipole emission of the $3p$ state, periodic in time delay with the full NIR optical cycle. In the 2DAS (panel d), this creates the line-like features near a Fourier energy corresponding to the NIR-photon energy.

Funding. Deutsche Forschungsgemeinschaft (DFG) (PF 790/1-1); European Research Council (ERC) (X-MuSiC-616783); Engineering and Physical Sciences Research Council (EPSRC) (EP/G055416/1).

REFERENCES

1. C. K. N. Patel and R. E. Slusher, Phys. Rev. Lett. **20**, 1087 (1968).
2. M. Schmitt, G. Knopp, A. Materny, and W. Kiefer, Chem. Phys. Lett. **270**, 9 (1997).
3. T. S. Rose and M. D. Fayer, Chem. Phys. Lett. **117**, 12 (1985).
4. S. Mukamel, *Principles of Nonlinear Optical Spectroscopy* (Oxford University, 1999).
5. D. M. Jonas, Annu. Rev. Phys. Chem. **54**, 425 (2003).
6. O. Golonzka, M. Khalil, N. Demirdöven, and A. Tokmakoff, Phys. Rev. Lett. **86**, 2154 (2001).
7. T. Brixner, J. Stenger, H. M. Vaswani, and M. Cho, Nature **434**, 625 (2005).
8. A. Halpin, P. J. M. Johnson, R. Tempelaar, R. S. Murphy, J. Knoester, T. L. C. Jansen, and R. J. D. Miller, Nat. Chem. **6**, 196 (2014).
9. I. V. Schweigert and S. Mukamel, Phys. Rev. A **76**, 012504 (2007).
10. I. V. Schweigert and S. Mukamel, Phys. Rev. Lett. **99**, 163001 (2007).
11. E. Sistrunk, J. Grilj, J. Jeong, M. G. Samant, A. X. Gray, H. A. Dürr, S. S. P. Parkin, and M. Gühr, Opt. Express **23**, 4340 (2015).
12. F. Bencivenga, R. Cucini, F. Capotondi, A. Battistoni, R. Mincigrucci, E. Giangrisostomi, A. Gessini, M. Manfredda, I. P. Nikolov, E. Pedersoli, E. Principi, C. Svetina, P. Parisse, F. Casolari, M. B. Danailov, M. Kiskinova, and C. Masciovecchio, Nature **520**, 205 (2015).
13. M. Chini, X. Wang, Y. Cheng, Y. Wu, D. Zhao, D. A. Telnov, S.-I. Chu, and Z. Chang, Sci. Rep. **3**, 1105 (2013).
14. B. Bernhardt, A. R. Beck, X. Li, E. R. Warrick, M. J. Bell, D. J. Haxton, C. W. McCurdy, D. M. Neumark, and S. R. Leone, Phys. Rev. A **89**, 023408 (2014).
15. L. Gallmann, J. Herrmann, R. Locher, M. Sabbar, A. Ludwig, M. Lucchini, and U. Keller, Mol. Phys. **111**, 2243 (2013).
16. C. Ott, A. Kaldun, L. Argenti, P. Raith, K. Meyer, M. Laux, Y. Zhang, A. Blättermann, S. Hagstotz, T. Ding, R. Heck, J. Madroñero, F. Martín, and T. Pfeifer, Nature **516**, 374 (2014).
17. C. Ott, A. Kaldun, P. Raith, K. Meyer, M. Laux, J. Evers, C. H. Keitel, C. H. Greene, and T. Pfeifer, Science **340**, 716 (2013).
18. C. Ott, A. Kaldun, P. Raith, K. Meyer, M. Laux, Y. Zhang, S. Hagstotz, T. Ding, R. Heck, and T. Pfeifer, "Quantum interferometry and correlated two-electron wave-packet observation in helium," arXiv:1205.0519 (2012).
19. H. Wang, M. Chini, S. Chen, C. H. Zhang, F. He, Y. Cheng, Y. Wu, U. Thumm, and Z. Chang, Phys. Rev. Lett. **105**, 143002 (2010).
20. M. Holler, F. Schapper, L. Gallmann, and U. Keller, Phys. Rev. Lett. **106**, 123601 (2011).
21. E. Goulielmakis, Z.-H. Loh, A. Wirth, R. Santra, N. Rohringer, V. S. Yakovlev, S. Zherebtsov, T. Pfeifer, A. M. Azzeer, M. F. Kling, S. R. Leone, and F. Krausz, Nature **466**, 739 (2010).
22. L. Argenti, Á. Jiménez-Galán, C. Marante, C. Ott, T. Pfeifer, and F. Martín, Phys. Rev. A **91**, 061403 (2015).
23. A. Blättermann, C. Ott, A. Kaldun, T. Ding, and T. Pfeifer, J. Phys. B **47**, 124008 (2014).
24. J. Mauritsson, T. Remetter, M. Swoboda, K. Klünder, A. L'Huillier, K. J. Schafer, O. Ghafur, F. Kelkensberg, W. Siu, P. Johnsson, M. J. J. Vrakking, I. Znakovskaya, T. Uphues, S. Zherebtsov, M. F. Kling, F. Lépine, E. Benedetti, F. Ferrari, G. Sansone, and M. Nisoli, Phys. Rev. Lett. **105**, 053001 (2010).
25. M. Lucchini, A. Ludwig, T. Zimmermann, L. Kasmi, J. Herrmann, A. Scrinzi, A. S. Landsman, L. Gallmann, and U. Keller, Phys. Rev. A **91**, 063406 (2015).
26. N. Shivaram, H. Timmers, X. M. Tong, and A. Sandhu, Phys. Rev. Lett. **108**, 193002 (2012).
27. P. Ranitovic, X. M. Tong, B. Gramkow, S. De, B. DePaola, K. P. Singh, W. Cao, M. Magrakvelidze, D. Ray, I. Bocharova, H. Mashiko, A. Sandhu, E. Gagnon, M. M. Murnane, H. Kapteyn, I. Litvinyuk, and C. L. Cocke, New J. Phys. **12**, 013008 (2010).
28. L. R. Moore, M. A. Lysaght, L. A. A. Nikolopoulos, J. S. Parker, H. W. van der Hart, and K. T. Taylor, J. Mod. Opt. **58**, 1132 (2011).
29. P. G. Burke and K. A. Berrington, *Atomic and Molecular Processes: An R-Matrix Approach* (IOP, 1993).
30. K. Schulz, M. Domke, R. Püttner, A. Gutiérrez, G. Kaindl, G. Miecznik, and C. Greene, Phys. Rev. A **54**, 3095 (1996).
31. A. Kramida, Y. Ralchenko, and J. Reader, and NIST ASD Team, "NIST Atomic Spectra Database (version 5.2)," National Institute of Standards and Technology, Gaithersburg, Maryland, 2014, Available: http://physics.nist.gov/asd [February 2, 2015].
32. G. Min, Z. Lin-Fan, L. Cun-Ding, and X. Ke-Zun, Chin. Phys. Lett. **25**, 3646 (2008).
33. D. Spence, J. Phys. B **14**, 129 (1999).
34. M. B. Gaarde, C. Buth, J. L. Tate, and K. J. Schafer, Phys. Rev. A **83**, 013419 (2011).
35. A. C. Brown, "Attosecond transient absorption of neon," 2015, http://dx.doi.org/10.17034/fa84d593-d1f2-4580-8419-fc7997871a80.
36. X. Wang, M. Chini, Y. Cheng, Y. Wu, X. M. Tong, and Z. Chang, Phys. Rev. A **87**, 063413 (2013).
37. S. Chen, M. Wu, M. B. Gaarde, and K. J. Schafer, Phys. Rev. A **87**, 033408 (2013).
38. W. C. Chu and C. D. Lin, Phys. Rev. A **85**, 013409 (2012).
39. K. Codling, R. P. Madden, and D. L. Ederer, Appl. Phys. Rev. **155**, 26 (1967).
40. U. Fano, Phys. Rev. **124**, 1866 (1961).
41. J. C. Slater, Phys. Rev. **36**, 57 (1930).
42. A. Blättermann, C. Ott, A. Kaldun, T. Ding, V. Stooß, M. Laux, M. Rebholz, and T. Pfeifer, Opt. Lett. **40**, 3464 (2015).
43. J. Mitroy, M. S. Safronova, and C. W. Clark, J. Phys. B **43**, 202001 (2010).